Journal of Materials Chemistry A

ROYAL SOCIETY OF CHEMISTRY

PAPER

View Article Online
View Journal

Check for updates

Cite this: DOI: 10.1039/d0ta07065c

A carbon–silica–zirconia ceramic membrane with CO_2 flow-switching behaviour promising versatile high-temperature H_2/CO_2 separation†

Sulaiman Oladipo Lawal, Liang Yu, Hiroki Nagasawa, Toshinori Tsuru and Masakoto Kanezashi *

Many researchers regard silica, silica-based and zeolite membranes as the agents that will accomplish H_2 separation. These membranes are expected to be productive in various mixture systems and under very high temperatures. This work reports the successful fabrication of a composite carbon–SiO_2–ZrO_2 ceramic membrane with a unique pressure-induced switching of CO_2 flows that allows versatile H_2/CO_2 separation at elevated temperatures. TG-MS, DTG-TGA, FT-IR, CP-MAS-^{13}C-NMR, and TEM provide corroborative evidence of the carbonization of starting material SiO_2–ZrO_2-acetylacetonate into C–SiO_2–ZrO_2. The resultant C–SiO_2–ZrO_2 displayed significant hysteresis in the CO_2 adsorption isotherm at a temperature well above the critical temperature of CO_2 (31 °C), which indicates structural conformation. Furthermore, single-gas permeation measurements showing upstream pressures of 200 and 500 kPa reveal different permeation values for CO_2 at 300 °C. In separating a H_2/CO_2 mixture at 50 and 300 °C under upstream pressures of 200 and 500 kPa, respectively, the flow of H_2 permeance reduces as the concentration of CO_2 increases in the feed side at 50 °C (1.14×10^{-8} down to 3.9×10^{-9} mol m^{-2} s^{-1} Pa^{-1} at 200 kPa). The pressure-induced surface flow of CO_2 at 300 °C and 500 kPa, however, reduces the hindrance to H_2 flow and results in H_2/CO_2 selectivity of ~20–30 for all CO_2 concentrations, which is on a par with molecular sieving membranes. This novel C–SiO_2–ZrO_2 material shows promise for many interesting applications.

Received 20th July 2020
Accepted 30th October 2020

DOI: 10.1039/d0ta07065c

rsc.li/materials-a

Introduction

Separation processes have already made a significant impact on the world.[1] The operating expenses of these processes, however, represent exorbitant investments of capital in industries such as petroleum, chemical, petrochemical, pharmaceutical, pulp, mineral and others.[2] Currently, about 80% of the world's energy demand is satisfied using fossil fuels.[3] These facts suggest that the world's industrial energy demand (and by extension fossil fuel consumption) derives from separation processes. By 2035, it is estimated that 8 countries (China, the USA, India, Brazil, Japan, South Korea, Canada, and Mexico) will demand as much as 5.24×10^{17} kJ (4.97×10^{17} BTU) of energy,[4] and 37% of that is estimated to come from the industrial sector alone of which about 79% is foreseen to be fossil fuel-derived by 2030.[5] Therefore, two interwoven problems must be solved: (1) reliance on fossil fuels; and, (2) energy requirement for industrial separation processes. Fortunately, new separation techniques such as membrane separation have been developed over the years to tackle these problems. The development of hydrogen separation membranes could be a two-pronged solution to the problems highlighted above.[6] On the one hand, membrane separation could be an energy-efficient way to separate H_2 from different mixtures,[2,7–10] while on the other hand the resultant H_2 could provide a sustainable and 'cheap' source of energy.[11,12]

Hydrogen production from the steam reforming of natural gas currently produces levels of production efficiency that average between 65 and 75%, which is the highest of all non-renewable production sources.[11] Currently, steam reforming of natural gas also has the lowest cost, uses existing infrastructure,[13] requires no oxygen for processing, and operates at the lowest temperature of all methods.[14] Obviously, steam reforming is the most widely used method for hydrogen production as it accounts for 80–85% of total hydrogen production.[15] As shown below, steam reforming of natural gas consists mainly of methane reforming and is basically accomplished in two steps:[6,16]

$$CH_4 + H_2O_{(g)} \rightarrow CO + 3H_2 \text{ (steam methane reforming step)}$$

$$CO + H_2O_{(g)} \rightarrow CO_2 + H_2 \text{ (water–gas shift step)}$$

The overall reaction becomes

$$CH_4 + 2H_2O_{(g)} \rightarrow CO_2 + 4H_2$$

Department of Chemical Engineering, Graduate School of Engineering, Hiroshima University, 1-4-1 Kagamiyama, Higashi-Hiroshima, 739-8527, Japan. E-mail: kanezashi@hiroshima-u.ac.jp

† Electronic supplementary information (ESI) available. See DOI: 10.1039/d0ta07065c

The final step in steam methane reforming (SMR) is separation of the effluent stream, which is comprised mostly of H_2, H_2O and CO_2, the composition of which depends on factors such as the reformer operating temperature and pressure and the steam-to-carbon ratio.[6,16] Techniques utilized for separation of H_2 from CO_2 and steam (for >99% pure H_2 stream) have traditionally consisted of venerable energy intensive approaches such as the pressure swing adsorption (PSA) of H_2 or CO_2, cryogenic distillation,[2,6,16,17] and the more recent process of energy conservative membrane separation.[6,16]

The composition of the final effluent gas stream is dependent on variable conditions such as temperature, pressure, and the steam-to-carbon ratio, which means that the separation technique of choice must be versatile enough to deal with these composition variations. This poses a challenge for the development of membrane separation techniques, and researchers must develop robust and versatile materials that simultaneously deliver the core targets of viable H_2 separation. Integrated gasification combined cycle applications (IGCC) also utilize the water–gas shift (WGS), and candidate materials must achieve levels of H_2 recovery and H_2/CO_2 selectivity of 70–90% and 21–62, respectively, under high temperatures and pressures,[18] although SMR/WGS targets in industrial sources of H_2 production have more stringent requirements for H_2 stream purity at >99.99%.[6,16,19] In addition to these targets, we believe taking H_2 separation membranes a step further would entail versatility in order to deal with H_2/CO_2 mixtures of widely varying compositions.

Several H_2 separation membranes that are applicable in a wide variety of temperature ranges have been developed over the years. The developers of these membranes have aspired to meet the set targets, and beyond, with varying degrees of success, which is associated with the material make-up of the membranes. Various H_2 separating membrane materials and processes have been reviewed.[2,6,20] Overall, H_2 separating membranes have yet to meet the desired potential, and as of recently, only two industrial applications of H_2 separation membranes are known to exist (recovery of H_2 from off-gases in the ammonia industry and production of pure H_2 in the electronic industry).[20] Thus, the principal driver of success in this quest is confined to creativity in materials research. An interesting group of materials that have received much attention in recent times are flexible metal–organic frameworks (FL-MOFs),[21–28] specifically because of their ability to structurally respond to external stimuli such as pressure, temperature, light and electric fields.[26] Such 'dynamic' responses are exploitable in separation processes. For example, a fluorinated MOF derived from a self-assembly of 2,2′-bis(4-carboxyphenyl) hexafluoro propane and zinc nitrate hexahydrate has shown high selectivity of CO_2 over N_2 because perfluorinated compounds exhibit electrostatic interactions with CO_2.[23] According to Kitagawa and Uemura,[21] a construction of 'dynamic' porous coordination polymers is rational *via* the placement of weak 'interaction devices' such as van der Waals force, π–π stacks and hydrogen bonds between stiff 1-D, 2-D and 3-D building blocks. This strategy offers a viable design for new porous materials by utilizing existing ceramic materials that have shown promise for H_2 separation. Thus, the 'interaction devices' employed must selectively engage with the mixture to be separated.

Composite SiO_2–ZrO_2 ceramic membranes have exhibited desirable levels of hydrothermal stability for H_2 separation, but expensive molecular sieving is required.[29] Hence, our group recently reported the successful chemical modification of a composite SiO_2–ZrO_2 ceramic membrane capable of molecular sieving.[30] This membrane in its ligand-modified form offered no promise for H_2/CO_2 separation. A successful modification with a chelating ligand of acetylacetone, however, has opened the possibility for *in situ* carbonization (pyrolysis of the organic ligand). If the deposited free carbon during pyrolysis approximates the anisotropic characteristics of graphite,[31] then the resultant van der Waals forces between the π–π stacks of carbon layers could serve as 'interaction devices' and endow new 'dynamic' characteristics into the SiO_2–ZrO_2 matrix. Van der Waals interactions could also develop between the carbon particles and the metal centers due to shifts in the electron densities. Moreover, a recent report of the carbonization of a molecular sieve silica membrane has introduced interesting properties to ordinary molecular sieve silica.[32,33]

Herein, we describe how SiO_2–ZrO_2-acetylacetonate was successfully pyrolyzed to form a carbonized form of SiO_2–ZrO_2 (hereafter called C–SiO_2–ZrO_2). Fig. 1 presents the expected pyrolysis and network formation pathway. The *in situ* carbonization was evaluated by characterization methods. C–SiO_2–ZrO_2 interaction with CO_2 at various temperatures was investigated *via* sorption experiments. Single and binary gas mixture experiments at 50 and 300 °C were performed to determine the permeation characteristics of H_2 and CO_2 as well as the separation performance of an alumina-supported C–SiO_2–ZrO_2 membrane. Finally, we discuss the place of a C–SiO_2–ZrO_2 membrane in the scheme of H_2 separation in industrial H_2 production systems and postulate as to the possibility that a versatile H_2 separation can be achieved. In the present study, we believe that we achieved a rational design for selective dynamism in a porous ceramic membrane.

Experimental

Preparation and pyrolysis of SiO_2–ZrO_2-acac powder and C–SiO_2–ZrO_2 membrane fabrication

The preparation of SiO_2–ZrO_2-acac sol was described in a previous work.[30] Briefly, a 5 wt% SiO_2–ZrO_2-acac polymeric sol

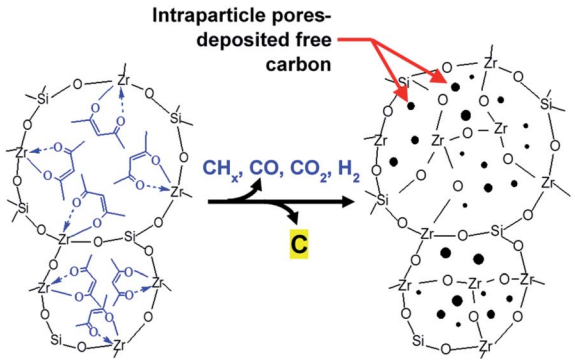

Fig. 1 Illustration of expected pyrolysis and network formation pathway of SiO_2–ZrO_2-acac to C–SiO_2–ZrO_2.

(referred to as SZa_4 sol in later sections) was prepared in two stages. In the first stage, a zirconium(IV) *tert*-butoxide solution (ZrTB, purity 80% in 1-butanol, Aldrich) was modified in ethanol (5 wt%) by coordinating with acetylacetone (Hacac, purity 99%, Aldrich) for one hour at room temperature, and the proportion of ZrTB/Hacac = 1/4. In the second stage, a 5 wt% solution of 98% pure tetraethoxysilane (TEOS, Aldrich) in ethanol was co-hydrolyzed and co-condensed with acetylacetone-modified zirconium(IV) *tert*-butoxide using deionized water and hydrochloric acid (37%, Nacalai Tesque) as a catalyst according to the following proportions: TEOS/ZrTB/H_2O/HCl = 1/1/4/0.25. Hydrolysis and poly-condensation were carried out by stirring the mixture in a closed vial at 500 rpm for more than 12 hours at room temperature.

SZa_4 (SiO_2–ZrO_2-acetylacetonate) powders were subsequently prepared from a SZa_4 sol by slowly drying the sol under an atmosphere controlled at 40–50 °C. Carbon–SiO_2–ZrO_2 powders were then prepared from SZa_4 powders *via* calcination in a 3-zone furnace at 550 or 750 °C under a N_2 stream at 600 ml min^{-1} for 20–25 min. For convenience the resultant pyrolyzed products will hereafter be referred to as CSZ550 or CSZ750 depending on the calcination temperature.

To prepare CSZ550 membranes, it was necessary to fabricate membrane supports. Details of this fabrication process have been previously reported.[34] Principally, the membrane supports were cylindrical α-alumina porous tubes (60% porosity, 1.2 μm pore size, outer diameter 1 cm, and length 10 cm; Nikkato Corporation, Japan) connected to closed and open non-porous supports at either end. The membrane support was comprised of additional graded layers of 2–3 μm α-alumina particles and 0.2 μm α-alumina particles that were coated onto the support in that order. The SiO_2–ZrO_2 intermediate layer was prepared using colloidal SiO_2–ZrO_2 sol, and has been previously described.[30] The coating of the SiO_2–ZrO_2 intermediate layer onto the α-Al_2O_3 particle layer was repeated 6–8 times to cover large pores from the α-alumina particle layers. Following this, to form the active separation layer, 1 wt% SZa_4 sol in ethanol was wipe-coated onto the SiO_2–ZrO_2 intermediate layer followed by calcination under a 600 ml min^{-1} nitrogen gas flow at 550 °C for 20–25 min in a 3-zone continuous flow furnace. This process was repeated 6–8 times to obtain the final defect-free CSZ550 membrane ready for single-gas and binary-mixture permeation measurements. It should be noted that after fabrication the CSZ550 membrane was kept in the membrane module under a He flow for 12 hours at 200 °C.

Characterization of materials

The pyrolysis route of the acetylacetonate ligand in SZa_4 powders was analyzed and monitored using thermogravimetry and mass spectroscopy (TGA-DTA-PIMS 410/S, Rigaku, Japan; DTG-60 Shimadzu Co., Japan) under nitrogen or He gas flows of 80 ml min^{-1} with a heating rate of 10 °C min^{-1}. In a similar manner, the combustion test for free carbon under air was performed using thermogravimetry (DTG-60 Shimadzu Co., Japan).

The presence and the chemical state of free carbon was confirmed using Fourier transform-infrared spectroscopy (FT-IR, FTIR-4100, JASCO, Japan) and solid-state ^{13}C cross polarization/dipolar decoupling magic-angle spinning nuclear magnetic resonance (CP/DD MAS-NMR), which was recorded using a NMR spectrometer (Varian 600PS, Agilent Inc., USA). ^{13}C-CP/DD MAS-NMR measurement was carried out at a frequency of 150.87 Hz using both ^{13}C–^{1}H dipolar coupling and decoupling modes. The spectra were acquired in 360 scans each with a 90° pulse of 3.2 μs and recycle delays of 70 s. Hexamethylbenzene was used as a reference against which the observed peaks were positioned, and a 6 mm zirconia rotor spun at a magic angle of 57.4° at 7 kHz contained the sample.

The physical evidence of the presence of carbon nanoparticles was confirmed by obtaining the micrographs of the SZa_4 and CSZ550 particles using transmission electron microscopy. The samples to be resolved were prepared on ultra-high-resolution carbon supports (STEM 100Cu Grids) by dropping approximately 10 μl of a 2 wt% dispersion of the fine particles in butanol onto the grids. Prior to examination, the prepared grids were vacuum-dried at 50 °C for 48 hours.

The crystal/amorphous structure and lattice spacing values of SZa_4 and CSZ550 powders were obtained using X-ray diffraction spectroscopy (D2 PHASER X-ray Diffractometer, Bruker, Germany) with Cu Kα as the radiation source at a wavelength of 1.54 Å. Furthermore, the sorption behaviors of CO_2 on both SZa_4 and CSZ550 powders were analyzed with CO_2 adsorption/desorption experiments carried out at 25, 30 and 35 °C. Prior to this measurement, samples of adsorbed gases and vapors were evacuated: SZa_4 at 100 °C and CSZ550 at 300 °C for at least 6 hours. Finally, temperature-programmed desorption of N_2 and CO_2 was carried out using a custom-built equipment setup fitted with a mass spectrometer (Dymaxion Dycor, Ametek Process Instruments, USA).

The cross-section morphology of the composite membrane was examined using Field Emission-Scanning Electron Microscopy (FE-SEM, Hitachi S-4800, Japan). Prior to examination, chipped samples of the membrane were attached to sample holders *via* carbon tape, and these were vacuum-dried at 50 °C for 24 hours.

Gas permeation measurement

A schematic representation of the gas permeation measurement setup is shown in Fig. S1.† Prior to the gas permeation measurement, a CSZ550 membrane was fitted into its module immediately after fabrication and placed inside the furnace in the gas permeation measurement rig at 200 °C under a moderate helium flow of 100 ml min^{-1} for about 12 hours to remove the adsorbed vapor. Single-gas permeation tests of the CSZ550 membranes were made using high purity gases (H_2, He, CO_2, N_2, CH_4, CF_4, SF_6 in that order). Each gas was fed to the upstream of the closed-end membrane module at 200–500 kPa of absolute pressure under temperatures ranging from 50–300 °C. Permeate side pressure was kept at atmospheric pressure and the permeate gas flow was measured using a bubble film flow meter (HORIBA-STEC, Japan).

Binary mixture separation performance was evaluated using the setup shown in Fig. S1† at 50 and 300 °C. In the measurement of binary gas mixture separation, H_2/CO_2 (80/20, 50/50, 20/

80) mixtures were fed to the upstream of the module while maintaining the pressure by setting the retentate side needle valve at 200 and 500 kPa with the downstream kept at atmospheric pressure. The compositions of the feed, retentate and permeate streams were analyzed using a pre-calibrated gas chromatograph (GC-14B, Shimadzu, Japan) equipped with a TCD detector (column: Porapak N (GL Science, Japan)). To evaluate the transmembrane pressure-drop of each component, the log mean pressure difference ($\Delta P_{i,lm}$) was applied (eqn (1)).

$$\Delta P_{i,lm} = \frac{\Delta P_{i,in} - \Delta P_{i,out}}{\ln(\Delta P_{i,in}/\Delta P_{i,out})} \quad (1)$$

In eqn (1), $\Delta P_{i,in}$ and $\Delta P_{i,out}$ represent the difference in partial pressures of component i between the retentate side and the permeate side at the inlet and outlet of the module, respectively.

Results and discussion

Carbonization of SiO_2–ZrO_2-acac into C–SiO_2–ZrO_2 and identification of the carbon state

In Fig. 2(a), the decomposition products of acac$^-$ (acetylacetonate) were confirmed *via* TG-MS (thermogravimetry-mass spectroscopy under an inert He atmosphere). In this figure the final decomposition temperature was around 500–550 °C, which corresponds to the profile for SiO_2–ZrO_2-acac thermal decomposition under an inert N_2 atmosphere, as presented in Fig. 2(b), which shows the DTG-DTA profiles for the thermal decompositions of SiO_2–ZrO_2-acac and C–SiO_2–ZrO_2 under N_2 and air, respectively. The final decomposition temperature for SiO_2–ZrO_2-acac under N_2 was approximately 500–550 °C with the DTA curve showing no exothermal peaks, which indicated no combustion reactions and possible deposition of non-volatile decomposition products. Under air, C–SiO_2–ZrO_2 (prepared by pyrolyzing SiO_2–ZrO_2-acac under N_2 at 550 °C for 20 minutes, as discussed under the Experimental section) showed thermal decomposition until the temperature reached

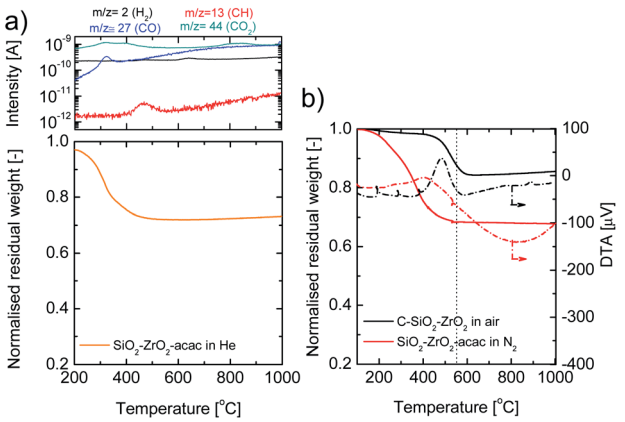

Fig. 2 Observed TG-MS profile of SiO_2–ZrO_2-acac under He (a) and TGA-DTA profiles of SiO_2–ZrO_2-acac under N_2 and C–SiO_2–ZrO_2 under air (b) (ramping rate: 10 °C min^{-1}).

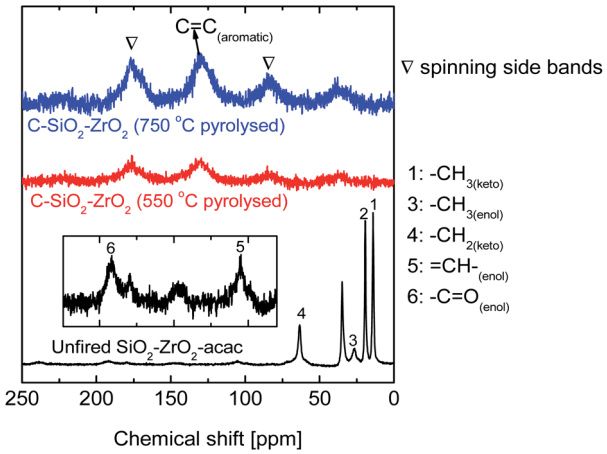

Fig. 3 CP-MAS-^{13}C-NMR spectra of fresh SiO_2–ZrO_2-acac powder and that pyrolyzed at 550 and 750 °C.

600 °C with exothermal peaks in the DTA curve indicating the combustion of deposited non-volatile carbon to CO and/or CO_2. The weight loss was calculated at 20%, which corresponded to 203 mg carbon/g of C–SiO_2–ZrO_2.

It is important to determine the state of carbon in the SiO_2–ZrO_2 matrix as this will aid in understanding the behavior of the composite material. Fig. 3 shows the change in the CP-MAS-^{13}C-NMR (cross polarization) spectra of the SiO_2–ZrO_2-acac transformation to C–SiO_2–ZrO_2 (pyrolyzed at 550 and 750 °C). For the spectrum of SiO_2–ZrO_2-acac, the different peaks indicate the intensity of the different functional groups of the enol and keto forms of the acac$^-$ chelate resulting from ^{13}C–^{1}H dipolar coupling. Acetylacetone in its keto tautomer form exists with two carbonyl groups (C=O), and as such is not able to properly chelate with transition metals. However, in its enol form, acetylacetone presents with one carbonyl group (C=O) and one enol group (C=C–OH) that more easily forms acetylacetonate, thus facilitating chelation. The magnified chemical shifts of peaks 5 and 6 on the SiO_2–ZrO_2-acac spectra show very small intensities indicating that the enol forms of acac$^-$ were adequately chelated to SiO_2–ZrO_2 by comparison with the spectrum of pure acetylacetone.[35] Furthermore, the spectra of 550 and 750 °C-pyrolyzed C–SiO_2–ZrO_2 showed broad peaks in the aromatic chemical shift region (~130 ppm) with two spinning side bands. The spinning side bands are peaks due to the chemical shift in anisotropy that is associated with sp^2 hybridized C species such as aromatic and carbonyl C.[36,37] This indicates the transformation of acac$^-$ into aggregated sp^2 hybridized graphitic carbon. The DD-MAS-^{13}C-NMR (dipolar decoupling mode) that resolved the magnetic environment of ^{13}C by decoupling ^{13}C–^{1}H revealed very sharp peaks (Fig. S2†). This is reasonable since free carbon has no bonded ^{1}H. The 550 and 750 °C-pyrolyzed C–SiO_2–ZrO_2 samples showed similar spectra, further indicating that pyrolysis up to 750 °C results in little or no change in the chemical and physical states of the pyrolysis product. The aromatic C=C bonds were also confirmed *via* FTIR (Fig. S3†).

The physical evidence of the presence of free carbon was obtained by transmission electron microscopy. Fig. 4(a)–(d)

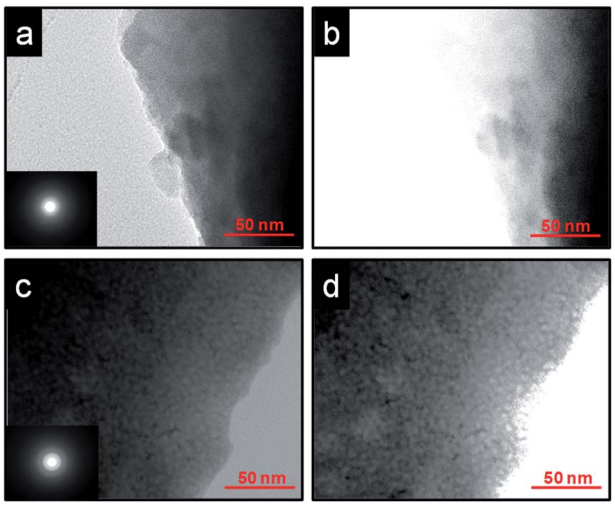

Fig. 4 TEM images of SiO_2–ZrO_2-acac: (a) original; (b) high-contrast and 550 °C-derived C–SiO_2–ZrO_2: (c) original; (d) high-contrast. Insets: electron diffraction images.

compare the electron diffraction patterns in the TEM micrographs of 50 nm-scale SiO_2–ZrO_2-acac (Fig. 4(a) and (b)) and C–SiO_2–ZrO_2 (Fig. 4(c) and (d)) that were used to detect the presence of carbon nanoparticles. Fig. 4(b) and (d) are high-contrast conversions of Fig. 4(a) and (c). The images show the edges of the particles. The micrographs reveal dark patches of several nanometers dispersed in the C–SiO_2–ZrO_2 matrix. Similar TEM images have been reported for fluorescent carbon nanoparticles (CNPs).[38] The inset images of both SiO_2–ZrO_2-acac and C–SiO_2–ZrO_2 show halo electron diffraction patterns indicating that the carbonization process had little effect on the amorphous structure of the SiO_2–ZrO_2 matrix.

Unique permeation properties of CO_2 in C–SiO_2–ZrO_2 membranes

Understanding the interaction between CO_2 and C–SiO_2–ZrO_2. Fig. 5(a) and (b) illustrate the observed evolution of the CO_2/C–SiO_2–ZrO_2 interaction. In Fig. 5(a), the adsorption isotherms of SiO_2–ZrO_2-acac and C–SiO_2–ZrO_2 powders at 25 and 35 °C are shown. Both samples show gentle Langmuir-like (almost Henry) type I adsorption isotherms in the pressure range observed. The adsorption–desorption isotherms of SiO_2–ZrO_2-acac at both 25 and 35 °C follow reversible paths indicating almost no special effect of CO_2 adsorption on neither the SiO_2–ZrO_2-acac structure nor the surface. In contrast, after carbonization of SiO_2–ZrO_2-acac resulted in C–SiO_2–ZrO_2, the adsorption–desorption isotherms of CO_2 showed significant hysteresis despite the smaller amount of adsorbed CO_2 indicating a structural conformation of the C–SiO_2–ZrO_2 to allow CO_2 adsorption. The existence of this hysteresis at a temperature above the critical temperature of CO_2 (31 °C) rules out the possibility of capillary condensation, and instead suggests this is the result of a structural transformation.[22] Culp *et al.*[22] proposed that when host–guest interaction can energetically compensate for the shape transformation of the host lattice, the host structure could conform to the shape of the guest molecules.

Fig. 5(b) presents the isosteric heat of the adsorption of CO_2 onto SiO_2–ZrO_2-acac and C–SiO_2–ZrO_2 calculated using the adsorption isotherms at 25, 30 and 35 °C and the Clausius–Clapeyron equation. The isosteric heat of CO_2 adsorption for C–SiO_2–ZrO_2 shows an average value of ~170 kJ mol^{-1} compared with ~34 kJ mol^{-1} for SiO_2–ZrO_2-acac. Lin *et al.*[39] calculated the theoretical potential energy surface (PES) barrier required for CO_2 chemisorption on a pristine graphite to be ~350 kJ mol^{-1} (~84 kcal mol^{-1}). With CO_2 adsorption on C–SiO_2–ZrO_2 releasing a maximum of ~290 kJ mol^{-1}, this suggests that CO_2 adsorption onto C–SiO_2–ZrO_2 can produce enough energy to deform the lattice structure to allow adsorption. The drastic decrease in the Q_{st} of C–SiO_2–ZrO_2 indicates an energetic heterogeneity of the C–SiO_2–ZrO_2 surface.

Fig. 6 shows the observed XRD patterns and lattice spacing values calculated from the centers of the amorphous peaks of SiO_2–ZrO_2-acac, C–SiO_2–ZrO_2, and pure SiO_2–ZrO_2 powders (with and without firing) measured at room temperature. The *d*-spacing value was reduced when SiO_2–ZrO_2-acac (0.356 nm) was

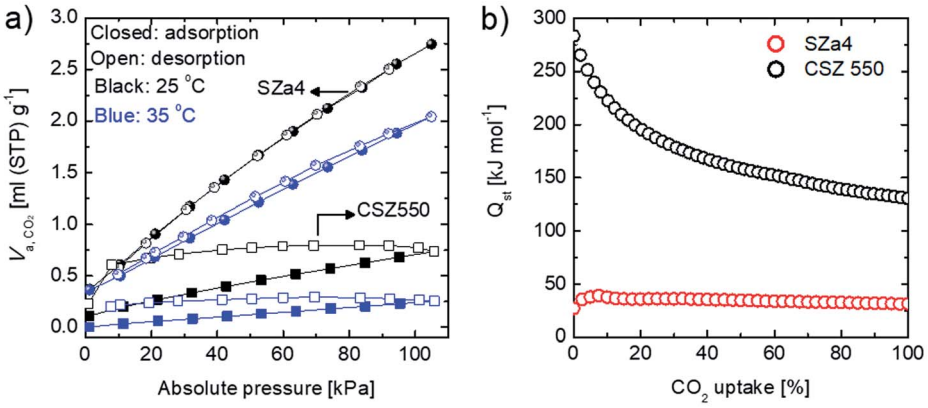

Fig. 5 (a) Adsorption–desorption isotherms of CO_2 onto SiO_2–ZrO_2-acac and C–SiO_2–ZrO_2 powders measured at 25 and 35 °C; (b) calculated isosteric heats of adsorption of CO_2 onto SiO_2–ZrO_2-acac and C–SiO_2–ZrO_2 powders using temperatures of 25, 30 and 35 °C.

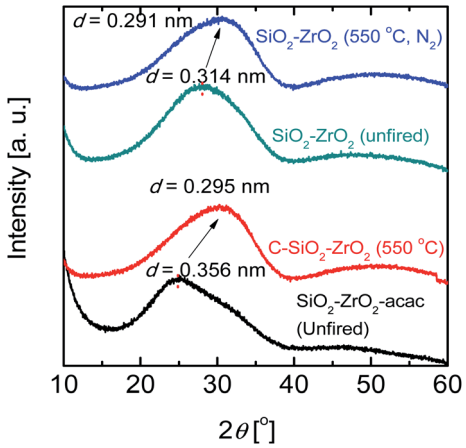

Fig. 6 Observed XRD patterns and calculated d-spacing values of SiO_2–ZrO_2-acac, C–SiO_2–ZrO_2 and pure SiO_2–ZrO_2 powders measured at room temperature.

pyrolyzed to C–SiO_2–ZrO_2 (0.295 nm) at 550 °C under N_2. On the other hand, pure SiO_2–ZrO_2 displayed a d-spacing shift from 0.314 nm to 0.291 nm after calcination at 550 °C. The resultant d-spacing of C–SiO_2–ZrO_2 was similar but somewhat higher in value compared with that of pure SiO_2–ZrO_2 (0.291 nm). The similar d-spacing values of C–SiO_2–ZrO_2 and pure SiO_2–ZrO_2 may suggest that free carbon layers are well integrated into the SiO_2–ZrO_2 lattice and do not form separate structures. The spacing between the successive layers of carbon can thus be safely assumed to be less than 0.295 nm. In Fig. 7, a scheme illustrating the interaction between CO_2 and C–SiO_2–ZrO_2 is shown. As established from characterization methods, free carbon is integrated in graphitic form in the C–SiO_2–ZrO_2 lattice. Graphitic carbon is anisotropic so that the layers of carbon are closely bound together in the vertical axis by weak van der Waals forces produced by delocalized π-orbital electrons (π–π stacking) and sp^2-hybridized C–C σ-bonding in the horizontal direction.[40] These delocalized electrons can induce dipole moments on approaching CO_2 molecules specifically because of the known vibrational modes of CO_2 which make it susceptible to dipole induction. The induced CO_2 molecules become attracted and electronically adsorbed onto the graphitic carbon layers thereby undergoing structural changes because the weak van der Waals forces allow the lattice to conform to the functionality of CO_2 guest molecules.[22]

Pressure-induced transition of CO_2 flow in C–SiO_2–ZrO_2 membranes. Preferential adsorption of CO_2 over other gases (such as N_2) onto C–SiO_2–ZrO_2 was established from N_2/CO_2-TPD measurements (Fig. S4†). A desorption curve can be observed at a temperature as high as 300 °C. Fig. 8(a) and (b) show the time courses for the single-gas permeance of He, H_2 and CO_2 at 50 and 300 °C, respectively, through an alumina-supported C–SiO_2–ZrO_2 membrane, as measured at an upstream pressure of 200 kPa. In both cases, a dynamic permeation trend is observed for CO_2 whereby the permeance reduces drastically with time before reaching a steady state. This points to a strong permeation hindrance to CO_2 flow due to blocking by adsorbed immobilized CO_2. At 50 °C, He and H_2 recovered about 65 and 79% of their initial values, respectively, after the feeding of CO_2, which effectively blocked certain pores due to adsorption by the C–SiO_2–ZrO_2 pores. This shows that adsorbed CO_2 has a blocking effect on the permeation paths of He and H_2 and that He, H_2 and CO_2 share the same permeation paths. At 300 °C the values for He and H_2 permeance are recovered at rates of 80 and 83%, respectively, and it would be safe to assume that the recovery ratio increases as temperature increases so that adsorption would be stronger at 50 °C than at 300 °C given the continued occurrence of adsorption.

Fig. 9(a) shows the single-gas permeance for a C–SiO_2–ZrO_2 membrane as a function of the kinetic diameter of different

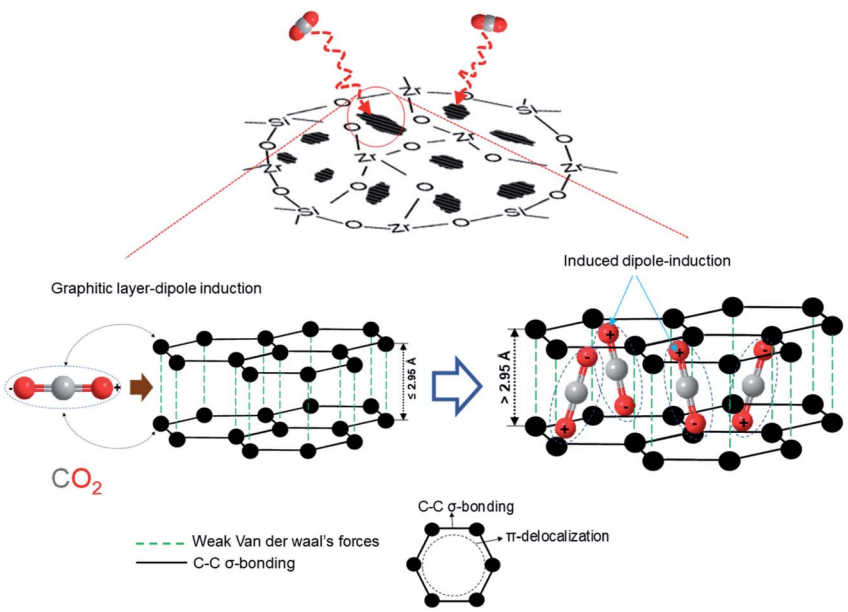

Fig. 7 Scheme illustrating the mechanism of the interaction between CO_2 and C–SiO_2–ZrO_2.

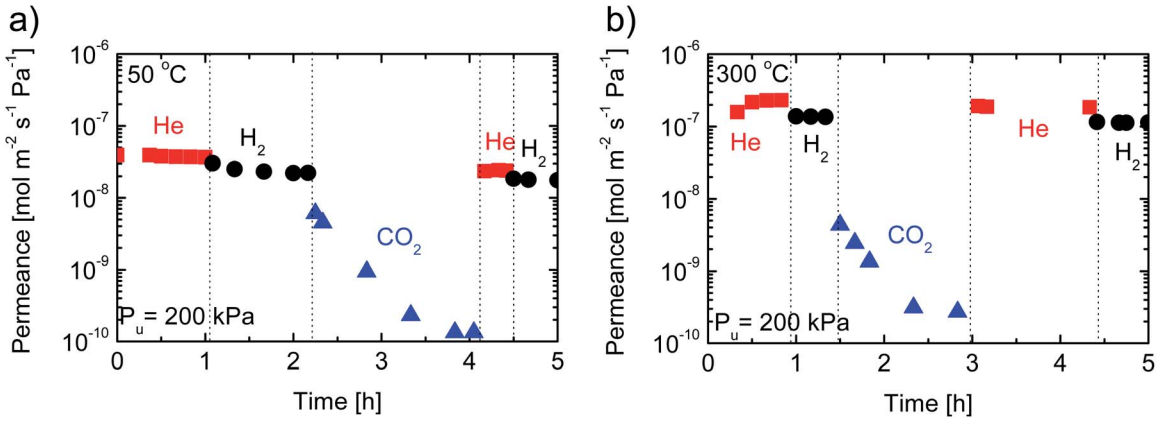

Fig. 8 Time courses for single-gas (He, H_2 and CO_2) permeation at 50 (a) and 300 °C (b).

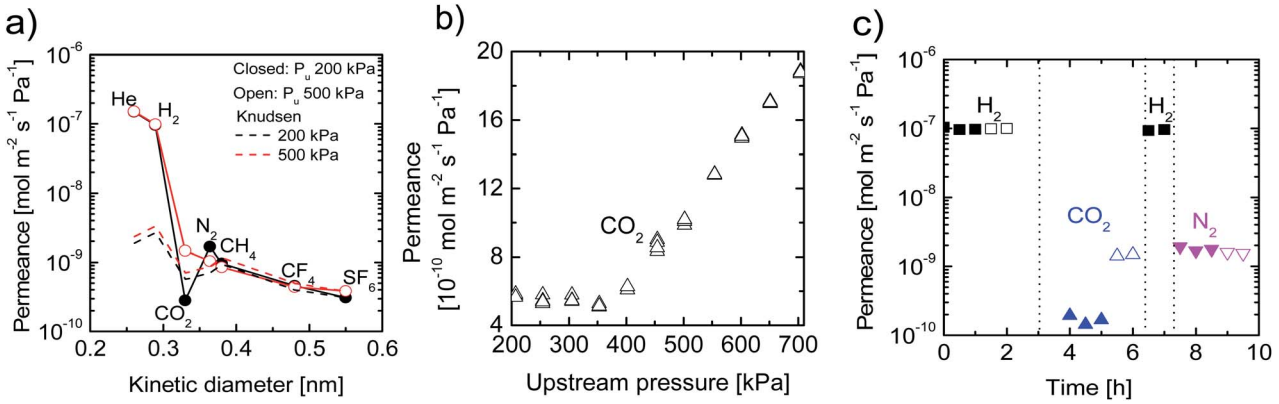

Fig. 9 (a) Single-gas permeance at 300 °C as a function of kinetic diameter at 200 and 500 kPa upstream pressures; (b) CO_2 permeance as a function of upstream pressure measured at 300 °C; (c) time course for the single-gas permeance of H_2, CO_2 and N_2 at 300 °C measured at upstream pressures of 200 and 500 kPa (closed symbols: 200 kPa; open symbols: 500 kPa).

gases (He (0.26 nm), H_2 (0.289 nm), CO_2 (0.33 nm), N_2 (0.364 nm), CH_4 (0.38 nm), CF_4 (0.48 nm), and SF_6 (0.55 nm)) measured at 300 °C under 200 and 500 kPa of upstream pressure. In evaluating the departure of a membrane's performance from Knudsen permeance to molecular sieving, the theoretical permeance based on SF_6 permeance *via* Knudsen diffusion is shown in Fig. 9(a), as indicated by the broken lines. The experimentally obtained values for He and H_2 permeance far exceeded those calculated *via* the Knudsen mechanism, which suggests the existence of pores so small that only H_2 and He could permeate them, which indicates a bimodal pore distribution in C–SiO_2–ZrO_2 membranes. It should be noted that pressures are presented in absolute values. For the measurement made at 200 kPa of upstream pressure, the gas permeance followed a trend such that permeance was decreased with an increase in the kinetic diameter, which generally indicates a molecular sieving property. CO_2 is the exception, and deviates from the trend with a permeance lower than other gases irrespective of the kinetic diameter. At 500 kPa of upstream pressure, however, gas permeance follows a trend whereby it decreases with an increase in the kinetic diameter without exception as opposed to gas permeance at 200 kPa. It was noted that values for gas permeance at 200 kPa remained either approximately the same (He, H_2, CH_4, CF_4, SF_6) at 500 kPa or somewhat less (N_2), but CO_2 permeance at 500 kPa (1.5×10^{-9} mol m^{-2} s^{-1} Pa^{-1}) was increased by almost one order compared with that at 200 kPa (1.7×10^{-10} mol m^{-2} s^{-1} Pa^{-1}). To further investigate this CO_2-specific trend, the pressure-dependence of CO_2 permeance was investigated using a fresh C–SiO_2–ZrO_2 membrane calcined at 550 °C, as shown in Fig. 9(b). The detailed time course of this experiment appears in Fig. S5.† The measurement was made multiple times to ensure steady-state values and to verify accuracy. The data presented in Fig. S5† are data recorded as soon as the CO_2 reached a steady state at 200 kPa. At subsequent pressures, the system response was quick, and a steady state was reached in a short time. In the initial feed of CO_2 gas to the upstream of the membrane at 200 kPa and 300 °C, a wait of approximately 2 hours was required for a steady state to be reached before recording the results as shown in Fig. S6.† The results obtained reveal that CO_2 permeance showed almost no dependence on upstream pressures that reached approximately 350 kPa. At 400 kPa and above, however, a positive slope in the permeance of CO_2 was almost linear with the slope of further increases in the pressure.

This is consistent with the kinetic diameter dependence of single gas permeance measurements made at 200 and 500 kPa. In some cases, this type of trend can be associated with the development of defects in a membrane.[41,42] The cross-sectional profile of the composite membrane taken with FE-SEM and shown in Fig. S7† suggests a defect-free C–SiO_2–ZrO_2 membrane layer with a thickness of about 20–40 nm, although the boundary between the C–SiO_2–ZrO_2 membrane layer and the SiO_2–ZrO_2 intermediate layer in not very clear. As shown in Fig. 9(c), however, after CO_2 permeation at 200 and 500 kPa, the permeance of H_2 recovered as much as 99% of its levels before CO_2 flow (after desorption of adsorbed CO_2 in vacuum at 350 °C). Furthermore, the values for N_2 permeation at 200 and 500 kPa showed similar values following CO_2 permeation, which is a sign of the absence of any defects. This suggests that the integrity of the membrane matrix was retained and was unaffected by the flow of CO_2. Therefore, it can be safely assumed that CO_2 only displayed a switching of flow regimes in the C–SiO_2–ZrO_2 membrane with 400 kPa being the transition pressure. Neither plasticization nor defects can be suggested in this case. It should be noted that since the measurement temperature (300 °C) was well above the critical temperature of CO_2 (31 °C), this phenomenon should not be ascribed to the flow of capillary condensate. We therefore suggest a pressure-induced multilayer diffusion mechanism. It has already been established in this section that adsorbed and immobilized CO_2 molecules prevent further permeation of gas-phase CO_2 molecules. This trend persists at low pressures. When the upstream pressure increases and the concentration of CO_2 exceeds a certain threshold where adsorbent–adsorbate interaction dominates, multi-layer adsorption may occur and thus lead to a greater mobility of gas-phase CO_2 molecules.[43]

Table 1 lists the calculations of activation energy for the temperature dependence of the gas permeation for different gases (H_2, CO_2, N_2 and SF_6), as regressed against eqn (2) and plotted in Fig. S8.† Based on these calculations, H_2 exhibited an activated diffusion mechanism with activation energy of 5.96 kJ mol^{-1}, while other gases showed Knudsen permeation with activation energies of less than 1 kJ mol^{-1}. In Fig. S8,† it is evident that the blocking effect of adsorbed CO_2 greatly contributes to a reduction in the apparent CO_2 permeance beyond the expected Knudsen value across the tested range of temperatures.

$$P_i = \frac{k_0}{\sqrt{M_i RT}} \exp\left(-\frac{E_{p,i}}{RT}\right) \quad (2)$$

Establishing the flow transition of CO_2 presents an interesting phenomenon whereby a C–SiO_2–ZrO_2 membrane could switch the flow of CO_2 based on a pre-designed threshold pressure. It is rational to assume that the threshold pressure for the transition of CO_2 flow would depend on the average pore size of the C–SiO_2–ZrO_2 membrane. Fine-tuning the average pore size to pre-design a threshold switching pressure, however, is a subject for future investigation. To establish the recyclability of CO_2-flow switching and the reliability of a C–SiO_2–ZrO_2 membrane over time, 3 cycles of the sequential pressure dependence of CO_2 permeance at 200 and 500 kPa upstream pressures were carried out at 300 °C for 16 hours, as shown in Fig. 10. The two regimes of CO_2 flow before and after transition were perfectly repeatable over the 3 cycles without a significant difference in permeance. Also, N_2 permeation was carried out to further stress the fact that the flow-switching behavior is specific to CO_2. The permeance of N_2 remained the same at 200 and 500 kPa, which indicated no pressure dependence for N_2 permeation through the C–SiO_2–ZrO_2 membrane. Both experiments further verified that no defects were formed during this switching of the CO_2 flow.

Table 1 Calculated activation energy for the permeation of different gaseous species through a C–SiO_2–ZrO_2 membrane regressed against eqn (2)

Gas	H_2	CO_2	N_2	SF_6
Activation energy [kJ mol^{-1}]	5.96	0.55	−0.88	0.88

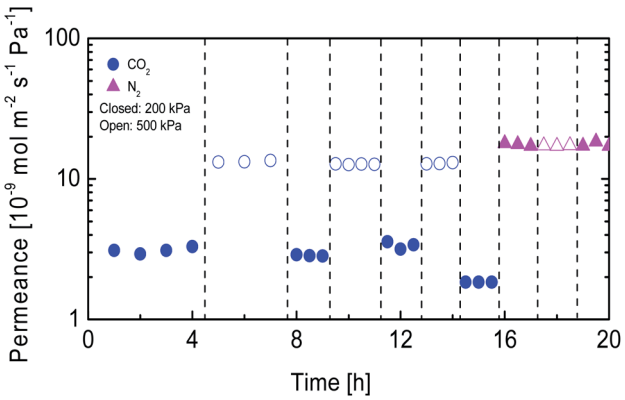

Fig. 10 Pressure-induced switching cycles of CO_2 flow represented by the time course of CO_2 and N_2 permeance under sequential pressurization at 200 and 500 kPa.

Binary H_2/CO_2 mixture separation performance of a C–SiO_2–ZrO_2-derived membrane

Effects of temperature, pressure and CO_2 feed mole fraction on the binary mixture separation performance. The detailed time courses of single- and binary-gas permeance through a C–SiO_2–ZrO_2 membrane are shown in Fig. S9.† Fig. 11(a) shows the values for the permeance of H_2 and CO_2 through a C–SiO_2–ZrO_2 membrane as a function of the CO_2 mole fraction in the feed (and by extension CO_2 upstream partial pressure) measured at 50 °C. At 50 °C and 200 kPa, H_2 and CO_2 permeance was decreased as the CO_2 mole fraction in the feed increased. This trend resembles that of silica membranes where the permeance of the adsorptive gas is expected to slightly increase as its mole fraction in the feed decreases.[44] The same trend was observed at 50 °C and 500 kPa. Fig. 11(b) illustrates the separation of a binary gas mixture of H_2 and CO_2 at 300 °C. At 200 kPa, the permeance of H_2 maintained a high value of 7×10^{-8} mol m^{-2} s^{-1} Pa^{-1} up to a CO_2 mole faction of 0.5 after which the

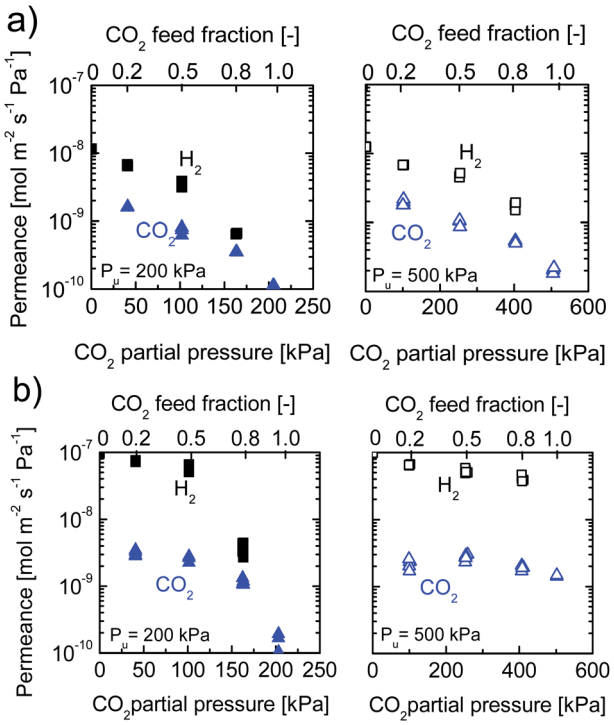

Fig. 11 Gas permeance as a function of CO_2 feed mole fraction and feed partial pressure at 50 °C (a) and 300 °C (b). Closed symbols: 200 kPa total upstream pressure; open symbols: 500 kPa total upstream pressure.

permeance was reduced drastically to 4×10^{-9} mol m^{-2} s^{-1} Pa^{-1} at a CO_2 mole faction of 0.8. At 500 kPa, however, only a slight decrease in H_2 permeance occurred even up to a CO_2 feed mole fraction of 0.8. This underscores the fact that at high values of both temperature and pressure, less CO_2 is adsorbed and the pressure-induced multilayer diffusion of CO_2 presents less of a hindrance to the permeation of H_2, and, thereby, high H_2/CO_2 selectivity is maintained across all levels of CO_2 concentration.

As mentioned earlier in this section, the permeance increase as the concentration of CO_2 in the feed decreased was similar to that observed for silica membranes in a surface diffusion mechanism. The increases in CO_2 permeance shown in Fig. 11(a) and (b), however, were more substantial. In addition, the permeance of the CO_2 in a binary mixture through the membrane was greater than that observed during single permeation at the same feed pressure. This can be explained by the fact that H_2 has a much higher flux than the slower permeating component CO_2, which exerts a 'sweeping' effect, and CO_2 is 'swept' along in the permeation paths. The same phenomenon was observed for a polypyrrolone membrane where the much slower permeating CH_4 molecules were 'swept' along by the much faster CO_2 molecules.[45]

Such a 'sweeping' effect can be explained by considering the co-existence of two gas species with different molecular sizes and adsorptive tendencies moving through a common permeation path. The molecules of the fast and less-adsorptive permeating gas continually collide with the slow permeating and more-adsorptive gas molecules and therefore displace them from the adsorbent surface thereby increasing the gas phase flow of the adsorbate gas molecules. Fig. 12 features a schematic illustration of the effect of H_2 presence on the adsorption-flux balance of CO_2 through C–SiO_2–ZrO_2 membrane pores. In the case of a binary mixture of H_2 and CO_2 gases, faster H_2 molecules sweep slower CO_2 molecules and therefore there is a considerable contribution of CO_2 to the overall bulk phase transport of the gas mixture. The fraction of the bulk mass flux contributed by each component in the gas mixture can be calculated based on a set of equations presented by Kamaruddin and Koros,[45] which compares to the gas-phase flux in single-gas permeation systems. A detailed derivation of these equations can be found in the ESI (eqn (S1)–(S5)).† When these equations were applied to single and binary H_2/CO_2 systems at 300 °C and 500 kPa, the results revealed that the fraction of the bulk-phase flux contribution by CO_2 is much higher in the permeation of a gas mixture than in that of pure CO_2 (Fig. S10†), which was predicted by Kamaruddin and Koros.[45]

Outlook on the practical application of a C–SiO_2–ZrO_2 membrane for H_2/CO_2 separation. There are reports of membranes that separate H_2 and CO_2 by utilizing strong CO_2 adsorption to create reverse CO_2/H_2 permselectivity at low temperature.[46] In this process, the more adsorptive CO_2 molecules permeate at the expense of blocked non-adsorptive H_2 molecules. In these membranes, as permeation temperature increases, molecular sieving properties dominate and achieve

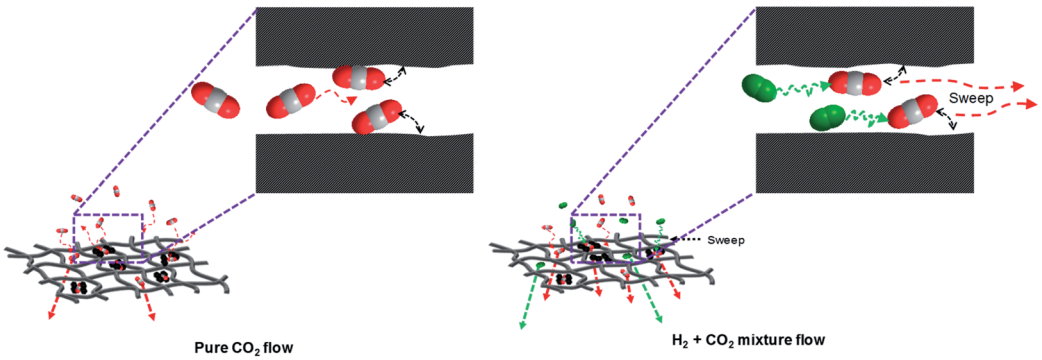

Fig. 12 Schematic illustration of the H_2 'sweeping' effect on CO_2 permeation.

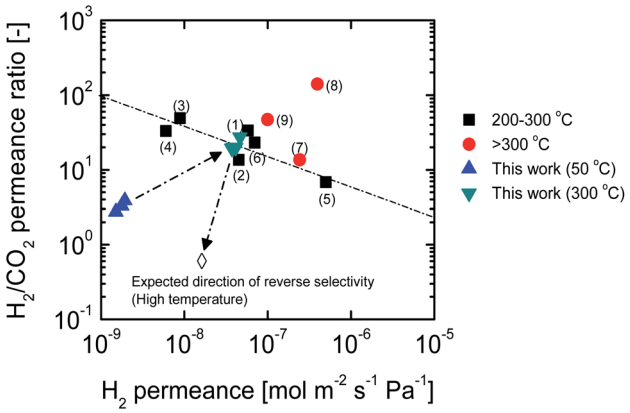

Fig. 13 Trade–off plot of H_2/CO_2 mixture selectivity *versus* H_2 permeance values for different high-temperature separation membranes.

a level of H_2 permselectivity that is suitable for high-temperature applications such as steam methane reforming/water–gas shift reactions (SMR/WGS) and the integrated gasification combined cycle (IGCC). In the present work, however, the molecular sieving properties at 300 °C with 200 kPa of upstream pressure seemed inadequate to achieve sufficient H_2 permselectivity across all CO_2 concentrations due to persistent CO_2 blocking. This is a drawback for practical and versatile high-temperature applications. This drawback is eliminated with a high pressure of 500 kPa where high H_2 permselectivity can be achieved across various CO_2 concentrations, as illustrated in Fig. 11(b). For practical high-temperature, high-pressure H_2/CO_2 separation purposes where membrane versatility may be of paramount importance as a result of fluctuating CO_2 concentrations, a C–SiO_2–ZrO_2 membrane could be useful. Fig. 13 compares the H_2 permeance-H_2/CO_2 mixture selectivity trade-off of high-temperature separation membranes (details in Table S1†). Most of the high-temperature H_2/CO_2 separation membranes include a range of versions from zeolitic to ceramic that achieve separation by means of molecular sieving (size exclusion of CO_2) of a 1 : 1 binary H_2–CO_2 mixture. Thus, it would be a novel occurrence to achieve comparable separation (good H_2 permeance-H_2/CO_2 selectivity trade-off) with a CO_2 adsorptive-type membrane across several H_2–CO_2 mixture ratios. Fig. 13 clearly shows that C–SiO_2–ZrO_2 membranes can achieve a separation performance that is comparable to many molecular sieving membranes at high temperatures even with most CO_2-concentrated feed stock. This ability is a result of the pressure-induced transition of CO_2 flow in C–SiO_2–ZrO_2 membranes (as previously established), which results in less hindrance to the flow of H_2 and promotes activated H_2 permeation.

Conclusions

In this work we set out to investigate the possible unique properties that could evolve during the *in situ* carbonization of acetylacetonate ligands in a SiO_2–ZrO_2 network and the resultant contribution to H_2/CO_2 separation. The *in situ* carbonization of SiO_2–ZrO_2-acac to C–SiO_2–ZrO_2 was confirmed by TG-MS, DTG-TGA, FT-IR, CP/DD-MAS-^{13}C-NMR, and TEM. The carbon content in C–SiO_2–ZrO_2 promoted the adsorption of CO_2, which resulted in a maximum heat of adsorption at 290 kJ mol^{-1} and provided energy sufficient to allow the carbon layers in C–SiO_2–ZrO_2 to conform to the CO_2 molecules. This development revealed that CO_2 could be trapped. The CO_2 permeance of the C–SiO_2–ZrO_2 membrane demonstrated a significant level of dependence on the feed pressure, but little dependence on either temperature or the CO_2 feed concentration under conditions of 300 °C and 500 kPa, which allowed for an interesting separation performance when used in binary H_2/CO_2 systems. The C–SiO_2–ZrO_2 membrane achieved a H_2/CO_2 separation performance comparable to molecular sieving membranes irrespective of the CO_2 feed content. In this study, we fabricated a two-parameter CO_2-switchable ceramic membrane. The switching parameters were the feed side pressure and the use of a fast permeating gas component.

Conflicts of interest

There are no conflicts to declare.

Acknowledgements

S. O. L. appreciates the support of the Japanese Government Ministry of Education, Culture, Science and Technology. In addition, the authors would like to thank Dr Maeda of the NBARD, Hiroshima University, for assisting with the TEM measurements and Dr Nakaya of the Department of Chemical Engineering and Applied Chemistry, Graduate School of Engineering, Hiroshima University, for assisting with the NMR measurements.

Notes and references

1 D. S. Sholl and R. P. Lively, *Nature*, 2016, **532**, 435.
2 R. W. Rousseau, *Handbook of Separation Process Technology*, John Wiley and Sons, New York, 1987.
3 S. Adhikari and S. Fernando, *Ind. Eng. Chem. Res.*, 2006, **45**, 875.
4 Y. Chang, J. Lee and H. Yoon, *Energy Policy*, 2012, **50**, 154.
5 E. A. Abdelaziz, R. Saidur and S. Mekhilef, *Renewable Sustainable Energy Rev.*, 2015, **15**, 150.
6 N. W. Ockwig and T. M. Nenoff, *Chem. Rev.*, 2007, **107**, 4078.
7 H. Li, Z. Song, X. Zhang, Y. Huang, S. Li, Y. Mao, H. J. Ploehn, Y. Bao and M. Yu, *Science*, 2013, **342**, 95.
8 T. Ji, Y. Sun, Y. Liu, M. Li, F. Wei, L. Liu, G. He and Y. Liu, *ACS Appl. Mater. Interfaces*, 2020, **12**, 15320–15327.
9 M. Kanezashi, D. Fuchigami, T. Yoshioka and T. Tsuru, *J. Membr. Sci.*, 2013, **439**, 78.
10 S.-J. Ahn, A. Takagaki, T. Sugawara, R. Kikuchi and S. T. Oyama, *J. Membr. Sci.*, 2017, **526**, 409.
11 E. Shoko, B. McLellan, A. L. Dicks and D. da Costa, *Int. J. Coal Geol.*, 2006, **65**, 213.
12 P. P. Edwards, V. L. Kuznetsov, W. I. F. David and N. P. Brandon, *Energy Policy*, 2008, **36**, 4356.

13 C. Acar and I. Dincer, *Int. J. Hydrogen Energy*, 2014, **39**, 1.
14 C. Acar and I. Dincer, *Int. J. Hydrogen Energy*, 2015, **40**, 11094.
15 D. R. Simbeck, *Presented at the 7th international conference on greenhouse gas control technologies (GHGT-7)*, Vancouver, British Columbia, Canada, September 6-10, 2004.
16 A. P. Simpson and A. E. Lutz, *Int. J. Hydrogen Energy*, 2007, **32**, 4811.
17 L. Barelli, G. Bidini, F. Gallorini and S. Servili, *Energy*, 2008, **33**, 554.
18 A. K. Ku, P. Kulkarni, R. Shisler and W. Wei, *J. Membr. Sci.*, 2011, **367**, 233.
19 J. J. Stanislowski, M. J. Holmes, A. C. Snyder, S. G. Tolbert and T. J. Curran, *Energy Procedia*, 2013, **37**, 2316.
20 S. C. A. Kluiters, *Presented under the 5th Research Framework Programme of European Union, Intermediate report EU project MIGREYD NNE5-2001-670*, Petten, December 2004.
21 S. Kitagawa and K. Uemura, *Chem. Soc. Rev.*, 2005, **35**, 109.
22 J. T. Culp, M. R. Smith, E. Bittner and B. Bockrath, *J. Am. Chem. Soc.*, 2008, **130**, 12427.
23 C. A. Fernandez, P. K. Thallapally, R. K. Motkuri, S. K. Nune, J. C. Sumrak, J. Tian and J. Liu, *Cryst. Growth Des.*, 2010, **10**, 1037.
24 A. Boutin, F.-X. Coudert, M.-A. Springuel-Huet, A. V. Neimark, G. Férey and A. H. Fuchs, *J. Phys. Chem. C*, 2010, **114**, 22237.
25 J. van den Bergh, C. Gücüyener, E. A. Pidko, E. J. M. Hensen, J. Gascon and F. Kapteijn, *Chem.–Eur. J.*, 2011, **17**, 8832.
26 J. Wang, J. Luo, J. Zhao, D.-S. Li, G. Li, Q. Huo and Y. Liu, *Cryst. Growth Des.*, 2014, **14**, 2375.
27 Z.-J. Li, J. Lu, M. Hong and R. Cao, *Chem. Soc. Rev.*, 2014, **43**, 5867–5895.
28 G. A. Craig, P. Larpent, S. Kusaka, R. Matsuda, S. Kitagawa and S. Furukawa, *Chem. Sci.*, 2018, **9**, 6463.
29 K. Yoshida, Y. Hirano, H. Fujii, T. Tsuru and M. Asaeda, *J. Chem. Eng. Jpn.*, 2001, **34**, 523.
30 S. Lawal, M. Kanezashi, H. Nagasawa and T. Tsuru, *J. Membr. Sci.*, 2020, **599**, 117844.
31 R. R. Dagastine, D. C. Prieve and L. R. White, *J. Colloid Interface Sci.*, 2002, **249**, 78.
32 M. C. Duke, J. C. Diniz da Costa, D. D. Do, P. G. Gray and G. Q. Lu, *Adv. Funct. Mater.*, 2006, **16**, 1215.
33 M. C. Duke, J. C. Diniz da Costa, G. Q. Lu, M. Petch and P. G. Gray, *J. Membr. Sci.*, 2004, **241**, 325.
34 W. Puthai, M. Kanezashi, H. Nagasawa, K. Wakamura, H. Ohnishi and T. Tsuru, *J. Membr. Sci.*, 2016, **497**, 348.
35 X. Tao, W. Qiu, H. Li and T. Zhao, *Polym. Adv. Technol.*, 2010, **21**, 300.
36 K. Ikeya and A. Watanabe, *Anal. Bioanal. Chem.*, 2016, **408**, 651.
37 J. C. C. Freitas, F. G. Emmerich, G. R. C. Cernicchiaro, L. C. Sampaio and T. J. Bonagamba, *Solid State Nucl. Magn. Reson.*, 2001, **20**, 61.
38 D. Pan, J. Zhang, Z. Li, C. Wu, X. Yan and M. Wu, *Chem. Commun.*, 2010, **46**, 3681.
39 S. C. Xu, S. Irle, D. G. Musaev and M. C. Lin, *J. Phys. Chem. B*, 2006, **110**, 21135.
40 D. D. L. Chung, *J. Mater. Sci.*, 2002, **37**, 1475.
41 B. A. McCool, N. Hill, J. DiCarlo and W. J. DeSisto, *J. Membr. Sci.*, 2003, **218**, 55.
42 S. Barma and B. Mandal, *Microporous Mesoporous Mater.*, 2015, **210**, 10.
43 J.-G. Choi, D. D. Do and H. D. Do, *Ind. Eng. Chem. Res.*, 2001, **40**, 4005.
44 M. Kanezashi, W. N. Shazwani, T. Yoshioka and T. Tsuru, *J. Membr. Sci.*, 2012, **415–416**, 478.
45 H. D. Kamaruddin and W. J. Koros, *J. Membr. Sci.*, 1997, **135**, 147.
46 M. Hong, S. Li, J. L. Falconer and R. D. Noble, *J. Membr. Sci.*, 2008, **307**, 277.